Energy and exergy analyses of direct ammonia solid oxide fuel cell integrated with gas turbine power cycle

F. Ishak, I. Dincer, C. Zamfirescu*

Faculty of Engineering and Applied Science, University of Ontario Institute of Technology, 2000 Simcoe Street North, Oshawa, Ontario, Canada L1H 7K4

ARTICLE INFO

ABSTRACT

This study presents the integration of direct ammonia solid oxide fuel cell with a gas turbine (DA-SOFC/GT) in a novel combined cooling, heating and power (CHCP) cycle. The integration strategy is compared for oxygen ion-conducting solid oxide fuel cells (SOFC-O) and hydrogen proton-conducting solid oxide fuel cells (SOFC-H). Unlike hybrid SOFC-absorption heat pumps, the current system is designed to exploit the refrigeration properties of ammonia to provide cooling with minimal bearing on complexity and capital cost. A system analysis is developed to cover both electrochemical and thermodynamic modelling. A detailed parametric study is also conducted to investigate the effects of varying the operating conditions and parameters on the energy and exergy efficiencies and the overall system performance. The results reveal that the SOFC-H integrated system offers better performance than that with the SOFC-O option. At an operating temperature of 1073 K and a pressure of 500 kPa, the respective energy and exergy efficiencies of the SOFC-H integrated cycle reach 81.1% and 74.3% compared to 76.7% and 69.9% for the SOFC-O. Under the same operating conditions, the cooling effectiveness of the system with both SOFC types becomes 14.7% based on the lower heating value (LHV) of ammonia.

© 2012 Elsevier B.V. All rights reserved.

1. Introduction

Despite the economic recession, the global market of SOFC systems is experiencing a robust growth with the expectation to increase from US$360 million in 2010 to US$530 million in 2016 [1]. This can be partly attributed to the growing awareness of the demonstrated high efficiency and the proven reliability of SOFC systems that position them as ideal candidates for applications of small to medium scale power generation and public transportation. The market opportunity can be further expanded by overcoming key technology barriers including cost of materials, fuel efficiency and effective hydrogen storage.

In our previous study [2], we examined the viability of using ammonia as a hydrogen carrier. The study also included a parametric analysis to compare the performance of two types of direct ammonia solid oxide fuel cells (DA-SOFC) based on the electrolyte used (i.e. SOFC-O or SOFC-H). The findings showed that both types of the DA-SOFC performed very well although hydrogen proton-conducting DA-SOFC demonstrated slightly better performance under all closed-circuit conditions. Accordingly, it was

concluded that ammonia is a highly efficient hydrogen storage medium and a suitable fuel for SOFC applications.

While the scientific community and industry continue to actively work on improving the SOFC efficiency and developing new SOFC materials, the synergy of combined heat and power (CHP) systems plays a vital role in the commercial viability and economic sustainability of SOFC technology.

A recent review conducted by Zhang et al. [3] presented many system integration schemes for coupling SOFC stacks with various bottoming cycles depending on the application of use. One interesting application discussed in the review is the integration of SOFC with absorption refrigeration system for the combined delivery of heating, cooling and power (CHCP). In spite of the versatility of such system, its main disadvantages include large volume, low cooling efficiency and high capital cost due to large number of components.

Zamfirescu and Dincer [4] proposed a hydrogen-fed integrated SOFC/GT system for vehicular applications. The performance of the system was assessed based on the optimization objective of maximum efficiency or maximum power density. Additionally, an exergy analysis was carried out to outline the major sources of exergy destruction in the system. It was found that the fuel cell stack can occupy about 75% of the total system volume and reduce the compactness of the system by 40% when the maximum system efficiency is achieved. They also concluded that the largest exergy

* Corresponding author. Tel.: +1 9059224455; fax: +1 9057213370.
E-mail addresses: fadi.ishak@uoit.ca (F. Ishak), ibrahim.dincer@uoit.ca (I. Dincer), calin.zamfirescu@uoit.ca, calinzam@gmail.com (C. Zamfirescu).

destruction occurred at the fuel cell stack and accounted for 60% of the total exergy destruction in the system.

Finally, another study by Dincer et al. [5] focused on the exergy analysis of an elaborate SOFC/GT system fuelled with methane. The study highlighted the advantage of higher operating voltage on the thermal and exergy efficiency of the system. It was also concluded that the highest thermodynamic irreversibilities emerged from the electrochemical and combustion processes. In particular, 37.1% of the total exergy destruction occurred in the fuel cell stack while 34.8% of the total exergy was destroyed in the combustion chamber.

The objective of this work is to propose integrated SOFC systems using ammonia as a direct fuel. A comparative assessment of oxygen ion-conducting solid oxide fuel cells (SOFC-O) and hydrogen proton-conducting solid oxide fuel cells (SOFC-H) is conducted. In order to demonstrate and evaluate these systems comprehensive energy and exergy analyses are conducted, and their energy and exergy efficiencies are assessed for practical applications. Also, energy and exergy efficiencies of a novel DA-SOFC/GT system are examined. Furthermore, a detailed parametric study is carried out to investigate the effects of design and operating conditions on the performance of the system.

2. Description and operational principle of the DA-SOFC

Regardless of the type of electrolyte material, fuel in the form of gaseous ammonia is subjected to catalytic dehydrogenation as it is fed through the anode channel of the DA-SOFC. The extracted hydrogen is then electrochemically oxidized in the fuel cell to produce electric power.

Depending on the thermodynamic equilibrium of the ammonia decomposition reaction at a given temperature and pressure, nitrogen gas may be produced in high concentration. The inert nitrogen can dilute the hydrogen concentration at the anode resulting in reduction of the reversible cell potential. The nitrogen produced is discharged from the anode compartment along with other gaseous effluents.

Fig. 1 depicts the configuration of the DA-SOFC with oxygen ion-conducting electrolyte. Oxygen from air is transported across the cathode layer to the cathode-electrolyte interface where it is reduced to oxygen ion. The oxygen ions are then transported through the electrolyte layer to electrochemically react with hydrogen at the anode-electrolyte interface. The water vapour produced by the reaction migrates to the anode channel thereby further reducing the hydrogen concentration. The water vapour exits the fuel cell along with unreacted fuel and other effluents.

The arrangement of the DA-SOFC with hydrogen proton-conducting electrolyte is shown in Fig. 2. Hydrogen is oxidized at the anode-electrolyte interface into protons and electrons. The protons are transported through the electrolyte layer to the cathode-electrolyte interface to undergo electrochemical reaction with oxygen from the cathode side. The water vapour produced by the fuel cell reaction is then transferred to the bulk gas in the cathode channel where it exits the cell with other effluents.
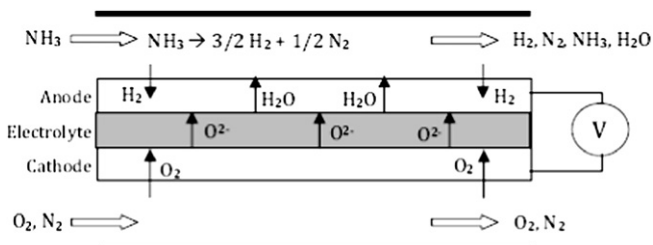

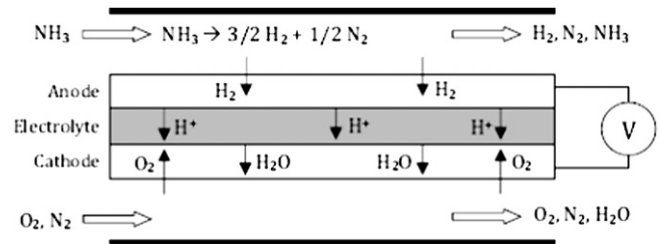Fig. 1. Schematic representation of the oxygen ion-conducting DA-SOFC.

Fig. 2. Schematic representation of hydrogen proton-conducting DA-SOFC.

This is a major advantage since hydrogen in the anode compartment is not diluted by the water vapour generated from the fuel cell reaction.

3. Description of integrated DA-SOFC/GT system

The DA-SOFC can be integrated with a bottoming thermodynamic cycle where the fuel cell is incorporated into a gas power system in a CHCP system. In the particular arrangement depicted in Fig. 3, the fuel tank contains pressurized ammonia for on-demand delivery to the system as needed. As the ammonia is extracted during the operation of the system, its temperature and pressure decrease by an amount proportional to its enthalpy of vaporization. In order to maintain the tank pressure at the desired level, a closed-loop heat exchanger (coil) is utilized to transfer rejected heat from a suitable fluid to the ammonia in the tank. As an added benefit, the heat transfer process and the refrigeration properties of ammonia are exploited to create a cooling effect in the medium flowing inside the closed-loop heat exchanger. This configuration provides a simple and cost-effective alternative to combined SOFC-Absorption refrigeration cycles.

The extracted ammonia is further heated in a two-stage heat exchanger arrangement (HX1 and HX2) to achieve a reasonable temperature before entering the fuel cell stacks. At this point, air is drawn into the compressor unit to be compressed to the desired pressure. Although the temperature of air rises during the compression process, further heating is achieved by passing the compressed air through a heat exchanger (HX3) upstream of the fuel cell stacks. The fuel and oxygen from air (oxidant) are electrochemically reacted inside the fuel cells to produce electric power while the heat generated due to thermodynamic irreversibilities is used for the thermal decomposition of ammonia and additional heating of the reactants and products.

As governed by the fuel utilization factor, a fraction of the hydrogen dissociated from the ammonia exits the fuel cell stacks along with other gaseous effluents to be burned in the adiabatic combustion chamber. The temperature of the gaseous mixture leaving the combustion chamber is sufficiently high for expansion and production of useful mechanical power in a gas turbine. Some of the power produced is used to drive the compressor while the remainder is used to drive an electric generator. The gas mixture leaving the turbine is split into two separate branches that feed the heat exchangers discussed earlier. Finally, heat is recovered from the exhaust gas which leaves the system through the recuperator at a moderate temperature.

4. Thermodynamic analysis

4.1. Thermodynamic equilibrium of ammonia decomposition

When heated, ammonia decomposes to hydrogen and nitrogen according to the following reaction:
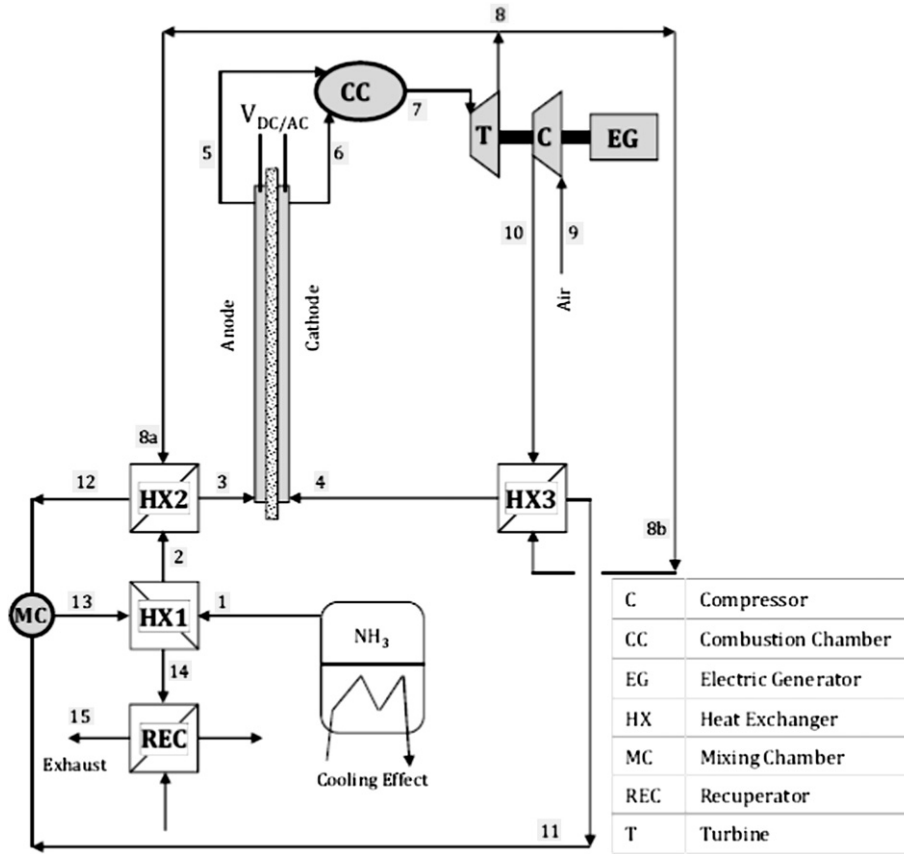
Fig. 3. Schematic diagram of integrated DA-SOFC/GT system.

$$NH_3 \leftrightarrow \frac{3}{2}H_2 + \frac{1}{2}N_2 \tag{1}$$

The above reaction is endothermic and depends on the temperature and pressure of the system among other factors. The reaction proceeds to the right as the temperature increases or to the left as the pressure increases thus producing less hydrogen. The thermodynamic equilibrium of ammonia can be obtained by minimizing the total Gibbs energy of the reaction:

$$(\Delta G_{system})_{T,P} = 0 \tag{2}$$

where the Gibbs energy of the system can be defined as the summation of the product of moles of chemical species i multiplied by the respective specific Gibbs energy at constant temperature and pressure

$$G_{system} = \sum n_i \bar{g}_i \tag{3}$$

The specific Gibbs energy can be described as the sum of the standard Gibbs function of formation and the chemical activity of a given species i. For real gases, the activity of species is defined as the ratio of its fugacity in the system to that at standard temperature and pressure (STP) conditions:

$$\bar{g}_i = \bar{g}_{fi}^0 + RT \ln \frac{f_i}{f_i^0} \tag{4}$$

If ideal or perfect gas conditions are assumed, the activity of the gaseous species is equal to its partial pressure in the system. For condensed matter (solid or liquid), the activity is equal to unity. Therefore, the total Gibbs energy of the system becomes

$$G_{system} = \left(\sum n_i \left[\bar{g}_{fi}^0 + \bar{R}T \ln(y_i P) \right] \right)_{gas} + \left(\sum n_i \bar{g}_{fi}^0 \right)_{condensed} \tag{5}$$

As an advantage of this method, chemical reactions need not to be specified. Instead, Gibbs energy minimization (GEM) requires data of the standard Gibbs function of formation of all chemical species which are expected to be involved or contribute to the thermodynamic equilibrium under consideration.

4.2. Cell-level thermodynamic and electrochemical modelling of SOFC

The equilibrium potential of any fuel cell is affected by the partial pressures of the chemical species involved in the electrochemical reaction. Under open-circuit conditions, the potential (voltage) can be written as

$$E = E^0 + \frac{\bar{R}T}{2F} \ln \left[\frac{p_{H_2} (p_{O_2})^{1/2}}{p_{H_2O}} \right] \tag{6}$$

where

$$E^0 = \frac{-\Delta G}{zF} \tag{7}$$

Furthermore, the examination of the potential of solid oxide fuel cells at closed-circuit conditions requires the characterization of the over-potentials affecting the cell operation. The working potential or voltage of SOFC can be characterized as

$$V = E - \varphi_{act,an} - \varphi_{act,ca} - \varphi_\Omega - \varphi_{conc,an} - \varphi_{conc,ca} \tag{8}$$

The activation over-potential is an irreversible loss related to the electrode kinetics and represents the difference between the actual potential (closed-circuit conditions) and the reversible potential (open-circuit conditions). The implicit relationship between the current density and the activation over-potential can be described using the Butler–Volmer expression [6]

$$J = J_0 \left[\exp\left(\frac{\alpha z F \varphi_{\text{act}}}{\overline{R}T} \right) - \exp\left(-\frac{(1-\alpha) z F \varphi_{\text{act}}}{\overline{R}T} \right) \right] \tag{9a}$$

The exchange current density (J_0) is a measure of the magnitude of electron activity at the equilibrium potential of the electrode. Its value is highly influenced by the electrode material, structure and other factors such as the temperature of the reaction and the length of the triple-phase boundary (TPB) [7]. The charge transfer coefficient (α) describes the effect of the electric potential on the ratio of the forward to the reverse activation barrier. For most electrochemical reactions in solid oxide fuel cells, this value is assumed to be 0.5 [8]. As such, the explicit relationship of the activation over-potential is

$$\varphi_{\text{act},\gamma} = \frac{\overline{R}T}{F} \sin h^{-1}\left(\frac{J}{zJ_{0,\gamma}} \right), \ \gamma = \text{anode, cathode} \tag{9b}$$

The electronic resistance of the fuel cell electrode and interconnect is usually very small and is considered negligible when compared to the ionic resistance of the electrolyte. The ionic resistance can be described by Ohm's law [9] as

$$\varphi_\Omega = J \delta R_\Omega \tag{10}$$

Here, the electrolyte resistance (R_Ω) is a function of the electrolyte properties and is highly dependent on the operating temperature.

The concentration over-potential accounts for losses incurred by the resistance of the porous electrode to the transport of gaseous species between the gas channel and the reaction sites at TPB. The mass transport in the electrodes is driven by the diffusion of reacting species due to concentration gradient as well as the permeation caused by the pressure gradient. Several mass transport models with varied accuracies have been used to capture the effects of concentration over-potential on the performance of fuel cells.

It has been previously demonstrated that the highest accuracy can be achieved using the dusty gas model (DGM) [10] and the mean transport pore model (MTPM) [11]. In particular, DGM visualizes the porous medium as a collection of large spherical particles suspended in space by external forces. The model takes into account the effects of diffusion and permeation mechanisms on the concentration of reacting species which is essential when modelling pressurized fuel cell systems. The one-dimensional multi-component mass transport DGM can be written as

$$\frac{N_i}{D_{i,k}^{\text{eff}}} + \sum_{j=1, j \neq i} \frac{y_j N_i - y_i N_j}{D_{ij}^{\text{eff}}} = -\frac{1}{\overline{R}T} \left[P \frac{dy_i}{dx} + y_i \frac{dP}{dx} \left(1 + \frac{B_0 P}{\mu_{\text{mix}} D_{i,k}^{\text{eff}}} \right) \right] \tag{11}$$

where the effective Knudsen diffusion accounts for the porosity and tortuosity of the electrode such that [12]:

$$D_{i,k}^{\text{eff}} = \frac{2}{3} \frac{\epsilon}{\tau} \sqrt{\frac{8\overline{R}T}{\pi M_i}} r_p \tag{12}$$

The effective binary diffusion of chemical species can be obtained using the Chapman-Enskog equation [13]:

$$D_{ij}^{\text{eff}} = 0.0018583 \frac{\epsilon}{\tau} \sqrt{T^3 \left(\frac{1}{M_i} + \frac{1}{M_j} \right)} \frac{1}{P \sigma_{ij}^2 \Omega_{D,ij}} \tag{13}$$

and the mean characteristic length (σ_{ij}) of the molecular collision diameter of species i and j is given by

$$\sigma_{ij} = \frac{(\sigma_i + \sigma_j)}{2} \tag{14}$$

The collision integral ($\Omega_{D,ij}$) is a function of temperature and the Lennard-Jones parameter (k/ε_{ij}) such that

$$\Omega_{D,ij} = \frac{1.06036}{\Gamma^{0.15610}} + \frac{0.19300}{\exp(0.47635\Gamma)} + \frac{1.03587}{\exp(1.52996\Gamma)} + \frac{1.76474}{\exp(3.89411\Gamma)} \tag{15}$$

where

$$\Gamma = \frac{kT}{\varepsilon_{ij}} \tag{16}$$

and

$$\varepsilon_{ij} = \sqrt{\varepsilon_i \varepsilon_j} \tag{17}$$

The values of the parameter in Eqs. (12)–(17) have been obtained from references [13] and [14]. The permeability of the porous electrode is estimated using the Kozeny–Carman relationship [15]

$$B_0 = \frac{4\epsilon^3 r_p^2}{72\tau(1-\epsilon)^2} \tag{18}$$

Furthermore, the viscosity of gas mixture can be calculated using the following semi-empirical equation [16]:

$$\mu_{\text{mix}} = \frac{\sum y_i \mu_i \sqrt{M_i}}{\sum y_i \sqrt{M_i}} \tag{19}$$

The gas viscosities are obtained from reference [13]. As presented by Zhu et al. [17], the summation of Eq. (11) enables the evaluation of the pressure gradient (dP/dx) across the electrode layer as

$$\frac{dP}{dx} = -\frac{\sum_{i=1} \left(\frac{N_i}{D_{i,k}^{\text{eff}}} \right)}{\left(\frac{1}{\overline{R}T} \right) + \left(\frac{B_0 P}{\mu \overline{R}T} \right) \sum_{i=1} \left(\frac{y_i}{D_{i,k}^{\text{eff}}} \right)} \tag{20}$$

At TPB, the molar flux of the gaseous reactants involved in the electrochemical reaction, namely hydrogen and oxygen, can be related to the current density as

$$N_i = \frac{J}{zF} \tag{21}$$

Depending on the type of electrolyte (SOFC-O or SOFC-H), the molar flux of water vapour can be calculated using Graham's law of diffusion which governs the diffusion process of gas mixtures [10]:

$$\sum_i N_i \sqrt{M_i} = 0 \tag{22}$$

The molar fluxes of all other non-reacting species are equal to zero [18]. Finally, the relationship between the concentration over-potential and the partial pressures can be written as [19]

- For SOFC-O:

$$\varphi_{\text{conc,an}} = \frac{\overline{R}T}{2F}\ln\left(\frac{p_{\text{H}_2}^{\text{TPB}}p_{\text{H}_2\text{O}}}{p_{\text{H}_2}p_{\text{H}_2\text{O}}^{\text{TPB}}}\right) \tag{23a}$$

$$\varphi_{\text{conc,ca}} = \frac{\overline{R}T}{4F}\ln\left(\frac{p_{\text{O}_2}}{p_{\text{O}_2}^{\text{TPB}}}\right) \tag{23b}$$

- For SOFC-H:

$$\varphi_{\text{conc,an}} = \frac{\overline{R}T}{2F}\ln\left(\frac{p_{\text{H}_2}}{p_{\text{H}_2}^{\text{TPB}}}\right) \tag{23c}$$

$$\varphi_{\text{conc,ca}} = \frac{\overline{R}T}{2F}\ln\left(\frac{p_{\text{H}_2\text{O}}^{\text{TPB}}\sqrt{p_{\text{O}_2}}}{p_{\text{H}_2\text{O}}\sqrt{p_{\text{O}_2}^{\text{TPB}}}}\right) \tag{23d}$$

4.3. Fuel and oxidant utilization

The utilization of ammonia can be defined in terms of the actual supply and consumption of the fuel or its hydrogen equivalent such that

$$U_f = \frac{(\text{Fuel})_{\text{consumed}}}{(\text{Fuel})_{\text{supplied}}} = \frac{(\text{H}_2)_{\text{consumed}}}{(\text{H}_2)_{\text{supplied}}} \tag{24}$$

Similarly, the utilization of air can be expressed as a function of the air supply and usage or its oxygen (oxidant) equivalent since air can be assumed to be composed of 79% nitrogen and 21% oxygen by volume.

$$U_o = \frac{(\text{Air})_{\text{consumed}}}{(\text{Air})_{\text{supplied}}} = \frac{(\text{O}_2)_{\text{consumed}}}{(\text{O}_2)_{\text{supplied}}} \tag{25}$$

4.4. Energy and exergy analyses of integrated system

At steady state operation, the energy balance of the system or any of its components can be written as

$$\dot{Q} - \dot{W} + \sum_i (\dot{n}_i\overline{h}_i)_{\text{in}} - \sum_i (\dot{n}_i\overline{h}_i)_{\text{out}} = 0 \tag{26}$$

The exergy associated with material flow is the sum of the physical and the chemical exergy

$$\dot{Ex} = \dot{Ex}_{\text{ph}} + \dot{Ex}_{\text{ch}} \tag{27}$$

where

$$\dot{Ex}_{ph} = \sum_i \dot{n}_i\left[(\overline{h}_i - \overline{h}_0) - T_0(\overline{s}_i - \overline{s}_0)\right] \tag{28}$$

$$\dot{Ex}_{ch} = \dot{n}\left[\sum_i y_i\overline{e}x_{\text{ch},i}^0 + \overline{R}T_0\sum_i y_i\ln y_i\right] \tag{29}$$

The previous expressions assume negligible change in kinetic and potential energies. In addition, the exergy of work is work itself; however, the exergy delivered by heat transfer is governed by the Carnot efficiency such that

$$\dot{Ex}_Q = \dot{Q}_j\left[1 - \frac{T_0}{T}\right] \tag{30}$$

In this study, the exergy is evaluated against reference temperature and pressure of 298 K and 101.325 kPa, respectively.

The exergy destruction due to thermodynamic irreversibilities in any component can be written as

$$\dot{Ex}_{D,\text{cmp}} = \sum_j \dot{Q}_j\left[1 - \frac{T_0}{T}\right] - \dot{W} + \sum_i (\dot{Ex}_i)_{\text{in}} - \sum_i (\dot{Ex}_i)_{\text{out}} \tag{31}$$

and the total exergy destruction in the system is

$$\dot{Ex}_{D,\text{total}} = \sum \dot{Ex}_{D,\text{cmp}} \tag{32}$$

The electric energy efficiency is dependent on the lower heating value of the fuel

$$\eta_e = \frac{\dot{W}_{\text{AC}} + \dot{W}_G}{\dot{n}\,\text{LHV}} \tag{33}$$

and the electric exergy efficiency can be written as

$$\psi_e = \frac{\dot{W}_{\text{AC}} + \dot{W}_G}{\dot{n}\overline{e}x_{\text{ch}}^0} \tag{34}$$

The total energy efficiency of the system is

$$\eta_t = \frac{\dot{W}_{\text{AC}} + \dot{W}_G + \dot{Q}_{\text{REC}}}{\dot{n}\text{LHV} + \dot{Q}_{\text{CL}}} \tag{35}$$

and the total exergy efficiency of the system is

$$\psi_t = \frac{\dot{W}_{\text{AC}} + \dot{W}_G + \dot{Ex}_{Q_{\text{REC}}}}{\dot{n}\overline{e}x_{\text{ch}}^0 + \dot{Ex}_{Q_{\text{CL}}}} \tag{36}$$

4.5. Energy and exergy analyses of system components

In this section, ideal gas conditions are assumed. Unless otherwise stated, all components and devices are considered to be well insulated to minimize heat losses to negligible levels. Furthermore, pressure losses have been ignored by virtue of component design.

- Fuel cell stack

The thermodynamic processes taking place inside the fuel cell module are depicted in Fig. 4. The ratio of hydrogen to ammonia entering the fuel cell is determined by the thermodynamic equilibrium and depends on the temperature and pressure of the corresponding reaction. Therefore, the heat generated by the isothermal electrochemical reaction of hydrogen and oxygen inside the fuel cell based on the molar flow of ammonia is

$$\dot{Q} = x\dot{n}U_fT_{\text{FC}}\Delta\overline{s} + I(\varphi_{\text{act,an}} + \varphi_{\text{act,ca}} + \varphi_{\text{ohm}} + \varphi_{\text{conc,an}} + \varphi_{\text{conc,an}}) \tag{37}$$

The generated heat is not only used for the internal thermolysis of fuel but also to supply sensible heat to the reactants and products. Furthermore, the temperature of all effluents is assumed uniform and equal to the fuel cell temperature. All surplus heat is rejected outside the fuel cell stacks. The thermal efficiency of the fuel cell stack can be written as

$$\eta_{\text{FC}} = \frac{W_e}{\Delta H} \tag{38}$$

and the exergy efficiency is

$$\psi_{\text{FC}} = 1 - \frac{\dot{Ex}_{D,\text{FC}}}{\sum_i (\dot{n}_i\overline{e}x_i)_{\text{in}} - \sum_i (\dot{n}_i\overline{e}x_i)_{\text{out}}} \tag{39}$$

Finally, the actual AC power produced by the fuel cell stack is

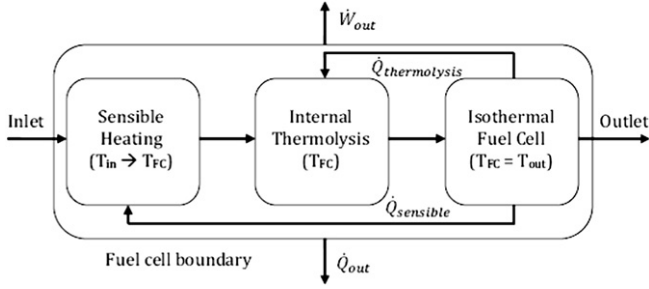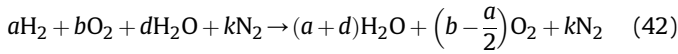$$\dot{W}_{\text{AC}} = \eta_{\text{INV}}\dot{W}_{\text{FC}} \tag{40}$$

Fig. 4. Thermodynamic processes of the fuel cell stack.

• Combustion chamber

Unreacted hydrogen and other effluents including excess air leave the fuel cell stacks and enter the combustion chamber where no work is done. It is also assumed that excess air ensures complete combustion. Applying the principles of energy and mass conservation on the component, yields

$$\sum_i (\dot{n}_i \bar{h}_i)_{\text{in}} = \sum_i (\dot{n}_i \bar{h}_i)_{\text{out}} \tag{41}$$

For the current system, this translates to

$$a\text{H}_2 + b\text{O}_2 + d\text{H}_2\text{O} + k\text{N}_2 \rightarrow (a+d)\text{H}_2\text{O} + \left(b - \frac{a}{2}\right)\text{O}_2 + k\text{N}_2 \tag{42}$$

Knowing the molar flow rate and the chemical composition of the combustion reactants and products, the adiabatic combustion temperature can be iteratively determined. Finally, the exergy efficiency of the combustion chamber is

$$\psi_{\text{CC}} = 1 - \frac{\dot{E}x_{D,\text{CC}}}{\sum_i (\dot{E}x)_{\text{in}}} \tag{43}$$

• Gas turbine

When the hot gaseous mixture leaves the combustion chamber and enters the gas turbine, it expands to deliver useful mechanical power. With the knowledge of the inlet temperature, the outlet temperature can be determined by

$$T_{\text{out}} = T_{\text{in}} \left(\frac{1}{\text{PR}}\right)^{(k-1)/k} \tag{44}$$

where

$$PR = \frac{P_{\text{in}}}{P_{\text{out}}} \tag{45}$$

$$k = \frac{\sum_i y_i \bar{c}_{p,i}}{\sum_i y_i \bar{c}_{v,i}} \tag{46}$$

The actual outlet temperature of the turbine is higher due to the effects of thermodynamic irreversibilities. The isentropic efficiency of the turbine can be applied to account for the difference such that

$$\eta_{s,T} = \frac{\sum_i (\dot{n}_i \bar{h}_i)_{\text{in}} - \sum_i (\dot{n}_i \bar{h}_i)_{\text{out}}}{\sum_i (\dot{n}_i \bar{h}_i)_{\text{in}} - \sum_i (\dot{n}_i \bar{h}_i)_{s,\text{out}}} \tag{47}$$

The actual temperature of gas mixture leaving the turbine can be iteratively determined from the actual enthalpy obtained. The exergy efficiency of the turbine can be written as

$$\psi_T = \frac{\dot{W}_T}{\sum_i (\dot{n}_i \bar{e}x_i)_{\text{in}} - \sum_i (\dot{n}_i \bar{e}x_i)_{\text{out}}} \tag{48}$$

• Air compressor

This component receives air at ambient temperature and pressure and compresses it to the desired pressure. This also results in an increase in the air temperature at the outlet of the compressor:

$$T_{\text{out}} = T_{\text{in}}(\text{PR})^{(k-1)/k} \tag{49}$$

where

$$PR = \frac{P_{\text{out}}}{P_{\text{in}}} \tag{50}$$

$$k = \frac{\sum_i y_i \bar{c}_{p,i}}{\sum_i y_i \bar{c}_{v,i}} \tag{51}$$

Similar to the gas turbine, the enthalpy of air at isentropic conditions can be related to its actual enthalpy through the isentropic efficiency of the compressor such that

$$\eta_{s,C} = \frac{\sum_i (\dot{n}_i \bar{h}_i)_{s,\text{out}} - \sum_i (\dot{n}_i \bar{h}_i)_{\text{in}}}{\sum_i (\dot{n}_i \bar{h}_i)_{\text{out}} - \sum_i (\dot{n}_i \bar{h}_i)_{\text{in}}} \tag{52}$$

from which the actual outlet temperature of air is iteratively obtained. The exergy efficiency of the compressor is

$$\psi_C = \frac{\sum_i (\dot{n}_i \bar{e}x_i)_{\text{out}} - \sum_i (\dot{n}_i \bar{e}x_i)_{\text{in}}}{\dot{W}_C} \tag{53}$$

• Electric generator

The surplus power representing the difference between the mechanical power generated by the turbine and that consumed by compressor can be captured using the back work ratio (BWR)

$$\text{BWR} = \frac{\dot{W}_C}{\dot{W}_T} \tag{54}$$

It is definitely desired to maintain this ratio as low as possible. The surplus power is used to drive an electric generator:

$$\dot{W}_G = \eta_G(\dot{W}_T - \dot{W}_C) \tag{55}$$

• Heat exchangers

Multiple gas-to-gas heat exchangers are utilized in this system. The effectiveness method [20] is used to determine the outlet temperature of the respective gaseous stream such that

$$\dot{Q} = \xi H_{C,\text{min}}(T_{h,\text{in}} - T_{c,\text{in}}) \tag{56}$$

where $H_{c,\text{min}}$ is the minimum heat capacity rate of the hot or the cold stream. As such, the outlet temperature of the hot stream is given as

$$\dot{Q} = \sum_i (\dot{n}_i \bar{c}_{p,i})_h (T_{h,\text{in}} - T_{h,\text{out}}) \tag{57}$$

and the cold stream

$$\dot{Q} = \sum_i (\dot{n}_i \bar{c}_{p,i})_c (T_{c,\text{out}} - T_{c,\text{in}}) \tag{58}$$

• Mixing chamber

Gas streams of different molar flow rates and temperatures flowing through different branches are mixed in a mixing chamber before entering heat exchanger (HX1). Under the assumption of adiabatic mixing of gases, the temperature of the gaseous mixture exiting the mixing chamber can be obtained from

$$\sum_i (\dot{n}_i \overline{h}_i)_{in} = \sum_i (\dot{n}_i \overline{h}_i)_{out} \qquad (59)$$

The exergy destruction can be determined from Eq. (31) while the exergy efficiency can be written as

$$\psi_{MC} = 1 - \frac{\dot{Ex}_{D,MC}}{\sum_i (\dot{n}_i \overline{ex}_i)_{in}} \qquad (60)$$

5. Results and discussion

The minimization of Eq. (5) was performed using the optimization function in MATLAB (MathWorks, Natick, MA, USA) [21]. In order to obtain the molar fractions and partial pressures of the reacting species at TPB, a computer code was developed using function (ode45) in MATLAB to numerically solve the set of simultaneous differential equations represented by Eq. (11). Furthermore, the required thermodynamic and chemical exergy data were obtained from references [22–24]. All thermodynamic calculations have been performed using EES (F-Chart Software, Madison, WI, USA) [25].

5.1. Thermolysis of ammonia in the DA-SOFC

The use of the GEM method revealed that the decomposition of ammonia is favoured at high temperature and low pressure as shown in Fig. 5. In particular, full conversion of ammonia can be achieved at a temperature of 700 K and atmospheric pressure. Nonetheless, it is well known that the kinetic rate of reaction is rather slow and often requires the use of a suitable catalyst to promote efficient conversion of ammonia. Complete conversion may be achieved over expensive metal catalysts such as ruthenium and platinum at temperatures around 600–650 K [26]; however, more economic alternatives include iron and nickel-based catalysts. Since the operating temperature of solid oxide fuel cells commonly ranges between 900 and 1400 K [27], it is safe to neglect the kinetic rate of reaction and assume that full decomposition of ammonia has been attained within the porous anode layer of the fuel cell.

5.2. Model validation

In the open literature, experimental investigations related to the DA-SOFC are scarce and rarely contain all the necessary information and parameters needed for model evaluation. Therefore, certain assumptions were made and some model parameters were adjusted to agree with the experimental data as reflected in Table 1. Ma et al. [28] conducted an experiment in which ammonia was used as a fuel in anode-supported SOFC-O with the arrangement of Ni-YSZ|YSZ|LSM-YSZ. The cell was tested at atmospheric pressure and different temperatures between 923 K and 1123 K. The performance of the cell was characterized by the high interfacial resistance which accounted for about 50% of the total resistance of the cell. The resistance of the electrolyte was also higher than expected at the same temperature as reported elsewhere [19,29]. In part, this can be attributed to the poor contact between the
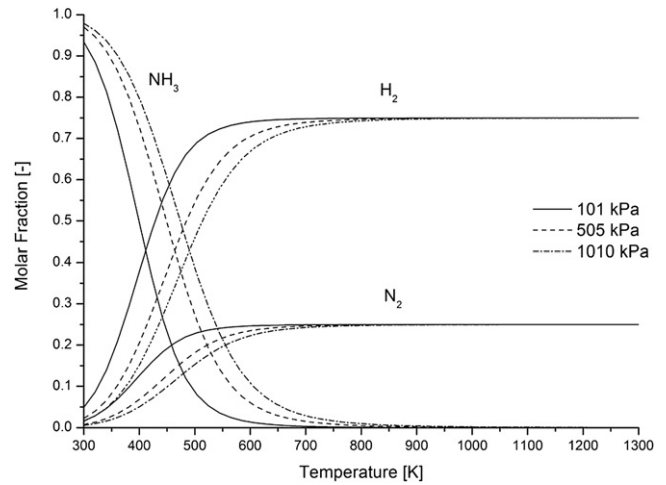
Fig. 5. Thermodynamic equilibrium of ammonia.

electrodes and the electrolyte as well as the microstructural properties of the cell components which are highly dependent on the processing method as discussed by Ringuede et al. [30]. The results in Fig. 6 show excellent agreement (within 2%) between the numerical simulation and the experimental data.

It is also worth noting that experimental tests are typically performed with low utilization of reactants in order to avoid the risk of local overheating and material degradation which can occur at high current densities. In practice, higher utilization factors are always desirable despite the lower efficiency and specific power output of the fuel cell stack.

5.3. Energy and exergy performance of integrated DA-SOFC/GT system

As noted earlier, it is desired to operate the fuel cell at the highest possible utilization factor while maintaining reasonable concentration of reactants and performance of the fuel cell. This value may vary between 80 and 95% for fuels and 20–35% for oxidants. Table 2 reflects the parameters used for the numerical simulation of the base case study. The polarization curve of the DA-SOFC is shown in Fig. 7. The peak power densities are 1875 W m^{-2} at 0.67 V for SOFC-O and 4507 W m^{-2} at 0.58 V for

Table 1
Parameters used in the validation of oxygen ion-conducting DA-SOFC.

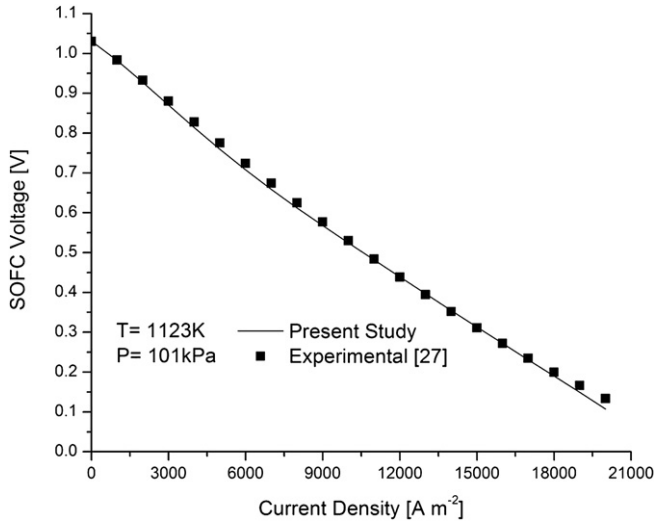| Parameter	Value
Operating temperature, T (K)	1123
Operating pressure, P (kPa)	101
Fuel utilization, U_f (%)	5
Oxidant (air) utilization, U_o (%)	5
Exchange current density of anode, J_{an} (A m^{-2})	$7 \times 10^9 \left(\frac{P_{H_2}}{p^0}\right)\left(\frac{P_{H_2O}}{p^0}\right)\exp\left(-\frac{100000}{RT}\right)$
Exchange current density of cathode, J_{ca} (A m^{-2})	$7 \times 10^9 \left(\frac{P_{O_2}}{p^0}\right)^{0.25}\exp\left(-\frac{130000}{RT}\right)$
Electrode porosity, ε	0.4
Electrode tortuosity, τ	4.25
Average pore radius of electrode, r_p (μm)	0.5
Resistivity of electrolyte, R_Ω (Ω m)	0.735
Anode thickness, (μm)	500
Electrolyte thickness, (μm)	30
Cathode thickness, (μm)	10

Sources [28,31–33].

Fig. 6. Comparison of simulation and experimental data of ammonia-fed SOFC-O.

Fig. 7. Polarization curve of oxygen ion and hydrogen proton-conducting DA-SOFC (base case).

SOFC-H. The significant difference of 144%, based on peak power density, was mainly due to the higher concentration of hydrogen at the anode of SOFC-H compared to that at the anode SOFC-O. This was also reflected by the difference in the open cell voltage as well as the detrimental impact of the concentration polarization which is most pronounced in the case of SOFC-O.

Furthermore, the respective fuel cell could not be operated at the corresponding peak power density due to the overall arrangement of integrated system and the heating requirements of the thermolysis of ammonia. The reduced operational voltages and current densities are listed in Table 3.

The temperature distribution of the system is depicted in Fig. 8 and the state points correspond to those in Fig. 3. For the base case study, the temperature of the fuel cell effluents was 1073 K (T5 and T6) and increased to 1193 K (T7) in the combustion chamber due to the adiabatic combustion of unused fuel. The hot exhaust gases entered the turbine and expanded to produce mechanical work and exited the turbine at 853 K (T8). At this point, the exhaust splits into two branches to deliver heating gas streams to the fuel and air heat exchangers.

The difference of 130 K between the temperature of the anode (T3) and the cathode (T4) inlets may potentially cause mechanical stresses which can lead to problems with sealing, leakage and cracking of ceramic components. This temperature mismatch can be explained by realizing that 95% of the turbine exhaust volume

was diverted as shown in Fig. 3 to heat exchanger (HX3) through branch (8a) in order to satisfy the high sensible heat demands of the incoming air. It also resulted in a low heat transfer rate in (HX2) that could not raise the temperature of the fuel to match that of the air entering the fuel cell.

The total specific electric power generated by the system with SOFC-H option was about 8% higher than that of the system with SOFC-O as given in Table 4. The difference corresponds to the lower exergy destruction in the system with SOFC-H option due to reduced thermodynamic irreversibilities. The tabulated data also revealed that more than 62% of the total power produced is delivered by the fuel cell stacks. This reasonable performance can be further improved by reducing the exergy destruction in the fuel cell.

In order to maintain the pressure of the ammonia exiting the tank at 505 kPa (with a saturation temperature of 277.3 K), heat was transferred from the closed-loop coil to the ammonia in the tank at a rate of 46.7 kJ mol^{-1} of ammonia. The heat rejection produced a cooling effect in the fluid passing through the coil with an effectiveness of 14.7% based on the LHV of ammonia.

Fig. 9 shows the exergy destruction within a system component as a percentage of the total exergy destruction of the power plant. It can be seen that the distribution of exergy destruction is very similar in both systems. The highest exergy destruction took place in the fuel cell stacks due to thermodynamic irreversibilities related to internal electrochemical processes as well as external losses due to the large thermal gradient between the fuel cell stack and its surroundings. Thus, the figure reiterates that efforts should be focused on high exergy destruction sites like the fuel cell module to minimize its thermodynamic losses and achieve maximum performance and efficiency.

Table 2
Parameters used for numerical simulation of the base case study.

Parameter	Value
Fuel utilization factor, U_f [%]	85
Oxidant utilization factor, U_o [%]	25
Stack temperature, T_{FC} [K]	1073
Stack Pressure, P_{FC} [kPa]	505
Pressure Ratio, PR	5
Cumulative cell area, A_{FC} [m^2]	250
Compressor efficiency, $\eta_{s,\,C}$ [%]	85
Turbine efficiency, $\eta_{s,\,T}$ [%]	90
Heat exchanger effectiveness, ξ [%]	90
AC generator efficiency, η_G [%]	95
DC/AC inverter, η_{INV} [%]	98
Ambient temperature, T_{amb} [K]	298
Ambient pressure, P_{amb} [kPa]	101.3
Composition of oxygen in air, [%]	21
Composition of nitrogen in air, [%]	79

Table 3
Operational voltages and current densities of the integrated system at different conditions.

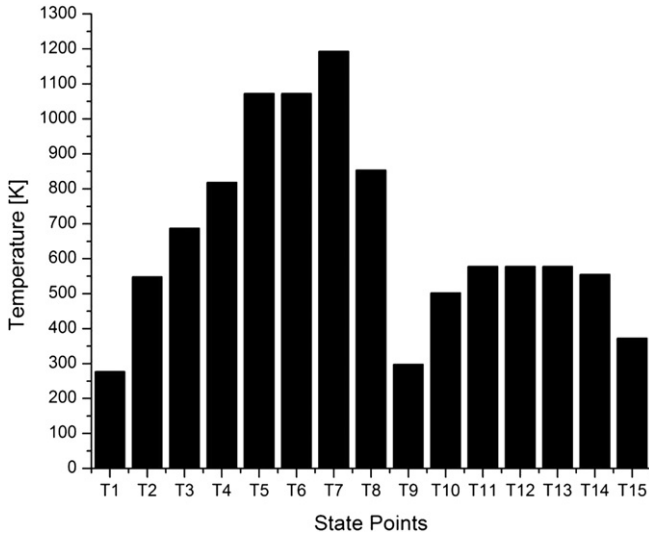| Fuel cell	SOFC-O		SOFC-H	
Parameters	V [V]	J [A m^{-2}]	V [V]	J [A m^{-2}]
Base case	0.52	3185	0.59	7640
T_{FC} = 1173 K	0.44	3545	0.52	7935
T_{FC} = 1273 K	0.36	3440	0.45	8200
U_f = 0.90	0.48	2190	0.55	6325
U_f = 0.95	0.43	1075	0.51	3670
PR = 2.5	0.69	2500	0.76	4110
PR = 7.5	0.44	3300	0.51	8650

Fig. 8. Temperature distribution of oxygen ion and hydrogen proton-conducting DA-SOFC/GT system (base case).

The first and second law efficiencies of the base case study are listed in Table 5. The data revealed the superiority of the system with SOFC-H option mainly due to its higher exergy efficiency when compared to that of SOFC-O. This difference is expected since SOFC-H boasted lower ohmic and concentration polarizations.

5.3.1. Effect of ammonia utilization

Fig. 10 reflects the effect of increasing the ammonia utilization in the fuel cell module on the total specific power of the plant and the back work ratio of the gas turbine-compressor assembly. Although the system with SOFC-H benefited from higher specific power in comparison to that with SOFC-O, both systems experienced considerable drop in specific power as the fuel utilization was increased. Consequently, the decrease in the molar flow rate of the gaseous mixture entering the gas turbine resulted in reducing the production of mechanical power. However, the required compressor power was also reduced at a different rate leading to a slight increase in the back work ratio.

In addition, Fig. 11 emphasizes the decreasing trend of energy and exergy efficiencies of the integrated system in response to the increase of ammonia utilization. It is therefore very important to optimize the fuel utilization of the system against the competing objective of maximum specific power.

5.3.2. Effect of fuel cell temperature

Increasing the operating temperature of the fuel cell resulted in appreciable decline of the total specific power as revealed in Fig. 12. At elevated temperatures, the system achieved lower operating power densities to allow for sufficient heat generation to satisfy the heating requirements of the reactants entering the fuel cell. Conversely, the higher temperature of the gaseous products increased the power production of the gas turbine hence the lower back work ratio.

Table 4
Specific power and exergy destruction in kJ mol^{-1} (base case).

		SOFC-O	SOFC-H
Overall system	Total specific power	203.6	219.5
	Total exergy destruction	100.0	83.5
Component	Specific power of fuel cell	126.0	141.9
	Specific power of electric generator	77.6	77.6
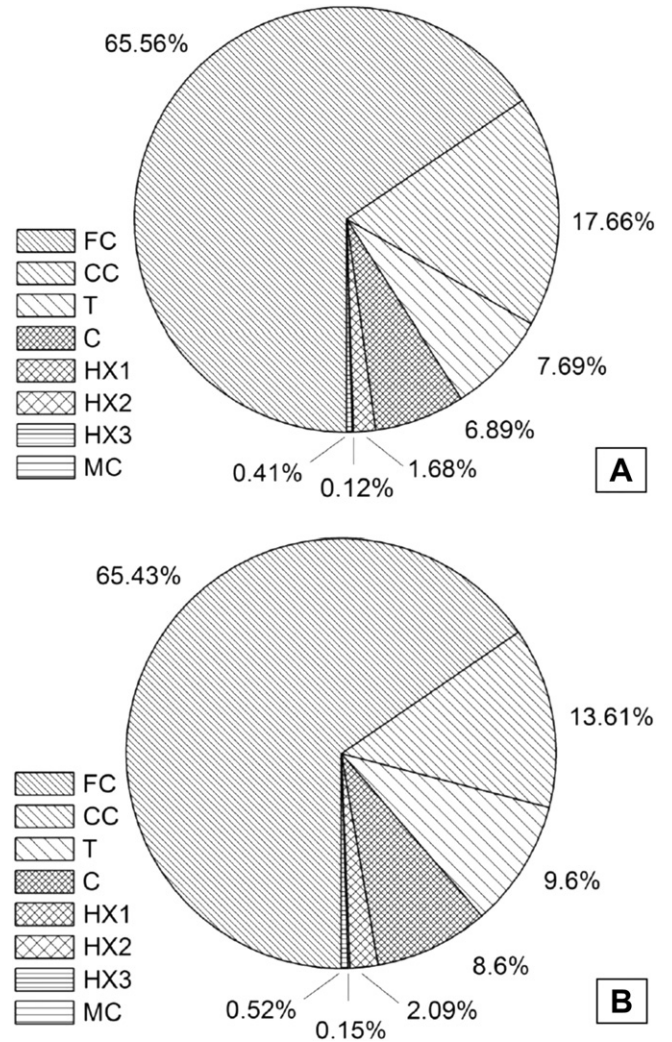
Fig. 9. The distribution of exergy destruction by system components (base case). Part A for SOFC-O option. Part B for SOFC-H option.

The effect of the fuel cell temperature on the efficiency of the systems is shown in Fig. 13. It can be observed that the system with SOFC-H option reflected superior performance and efficiency in comparison to that coupled with SOFC-O. As the temperature of the fuel cell increased, the electric energy and exergy efficiencies degraded due to lower specific power. Notwithstanding, the higher temperature of the gaseous products boosted the amount of recoverable heat and the associated exergy leading to an overall increase in the total energy and exergy efficiencies of the respective system.

Table 5
Energy and exergy efficiencies of the DA-SOFC/GT system (base case).

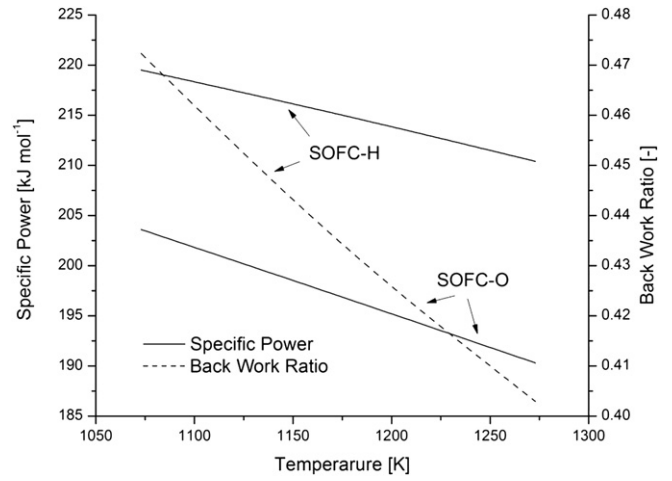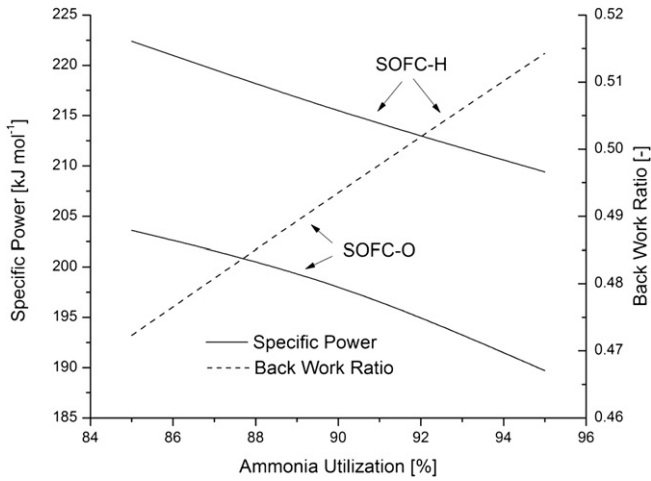|		SOFC-O	SOFC-H
Overall system	η_t	76.7	81.1
	ψ_t	69.9	74.3
	η_e	64.3	69.3
	ψ_e	60.2	65.0
Component	ψ_{FC}	66.7	76.6
	ψ_{CC}	93.6	96.0
	ψ_T	95.1	95.1
	ψ_C	90.2	90.2
	ψ_{Hx1}	61.2	61.2
	ψ_{Hx2}	96.4	96.4
	ψ_{Hx3}	99.3	99.3

Fig. 10. Effect of ammonia utilization on the total specific power and back work ratio of the system.

Fig. 12. The effect of increasing the fuel cell temperature on the total specific power and back work ratio.
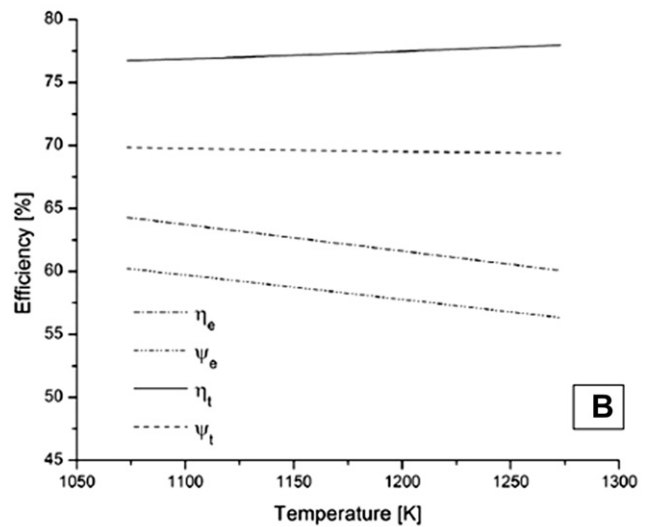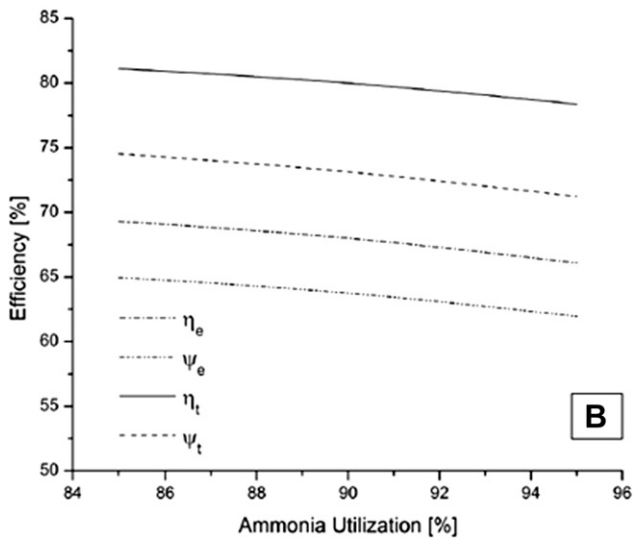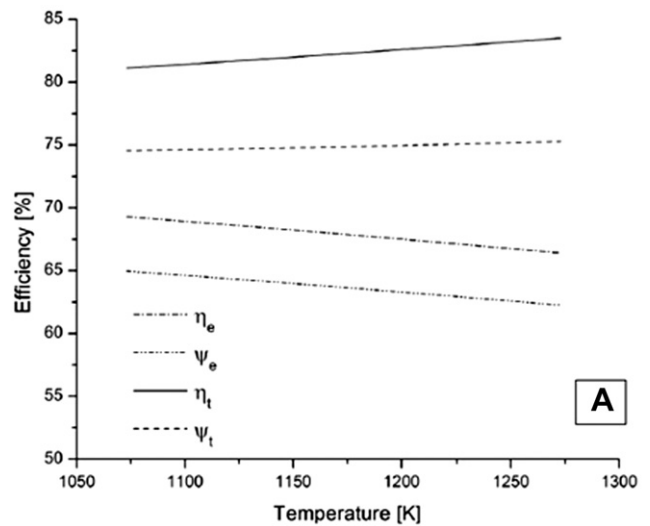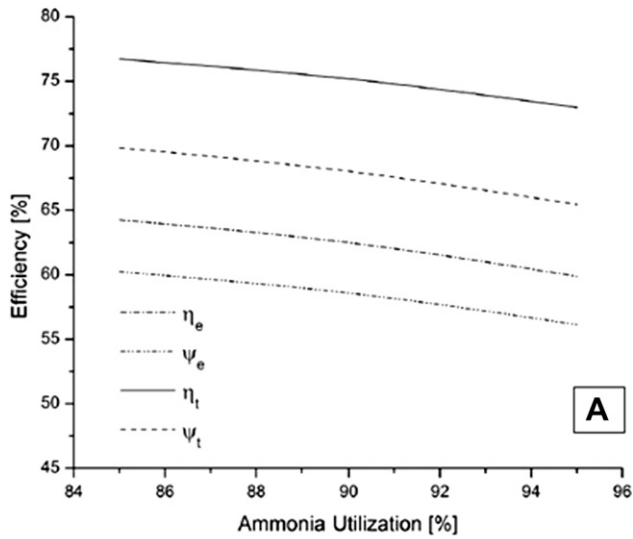

Fig. 11. Effect of ammonia utilization on the energy and exergy efficiency of the system. Part A for SOFC-O option. Part B for SOFC-H option.

Fig. 13. The effect of increasing the fuel cell temperature on the efficiency of the system. Part A for SOFC-O option. Part B for SOFC-H option.
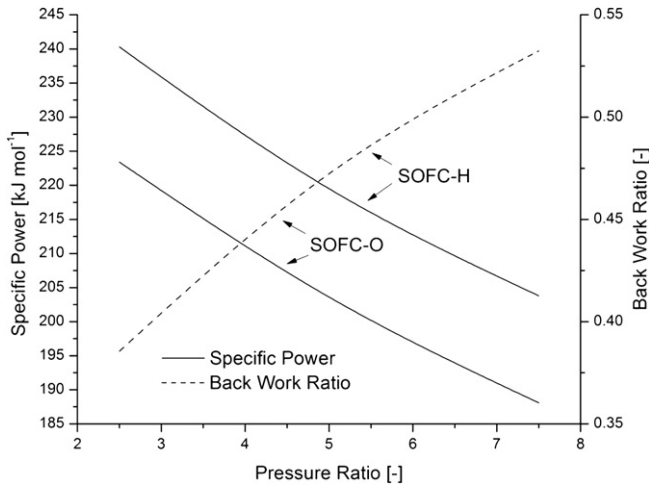
Fig. 14. The effect of pressure ratio on the total specific power and back work ratio of the integrated system.
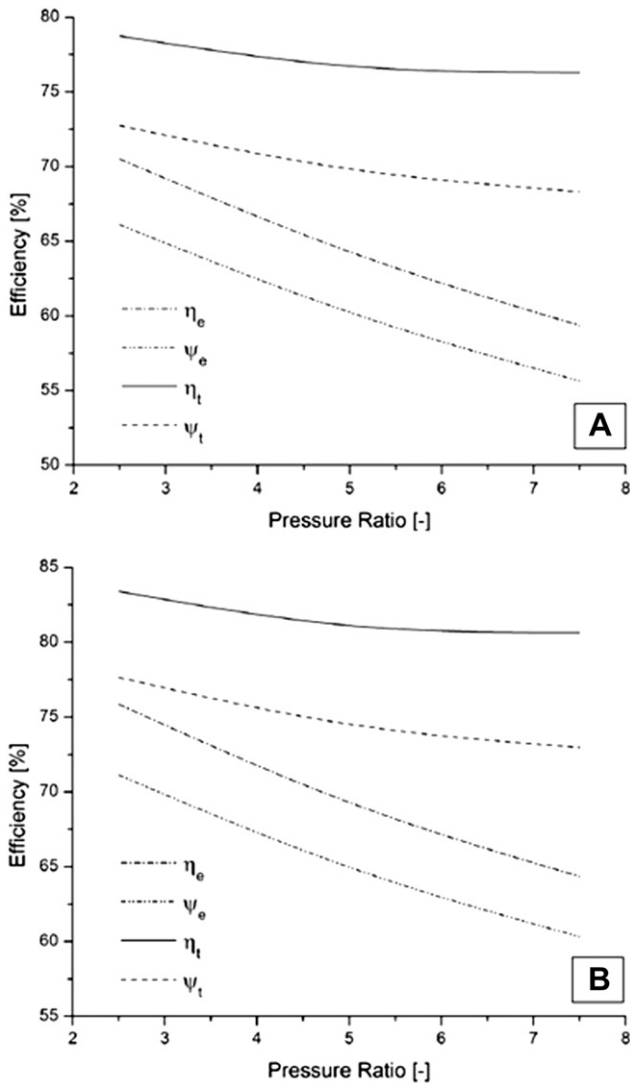
Table 6
The effect of pressure ratio on the cooling performance of ammonia of the integrated system.

	Pressure ratio		
	2.5	5.0	7.5
Tank temperature [K]	259.5	277.3	289
Cooling load [kJ mol^{-1}]	47.3	46.7	46.3
Effectiveness [%]	14.9	14.7	14.6

5.3.3. Effect of pressure ratio

In our previous work [2], we demonstrated that increasing the operating pressure enhanced the performance of solid oxide fuel cells. However, Fig. 14 reflects the adverse impact of increasing the operating pressure of the integrated system on the total specific power and the back work ratio. This indicates that a significant portion of the mechanical power produced is drawn by the air compressor thereby reducing the net electric power generated per unit mole of fuel. Accordingly, the system suffered a considerable decline in the electric energy and exergy efficiencies within the studied range as shown in Fig. 15. Nonetheless, the ratio of recoverable heat from the recuperator to that added to the ammonia tank increased proportionally with the increase of the pressure ratio. In this manner, the reduction of the overall energy and exergy efficiencies was less pronounced at higher pressure ratios.

It is also worth mentioning that the cooling performance of the system is strongly affected by the pressure ratio as demonstrated in Table 6. Although the cooling load capacity and effectiveness remained virtually unchanged, the refrigeration or cooling potential may be diminished due to negative impact of increasing the operating pressure of the system on the saturation temperature of ammonia.

5.3.4. Effect of reference state

Exergy is a property of the system and its environment. Fig. 16 depicts the effect of changing the reference temperature on the exergy efficiencies of the integrated system. While the effect is negligible on the exergy efficiency based on electric power production, the total exergy efficiency suffers a minor drop over the studied range. The reduced efficiency is proportional to the decrease in exergy associated with the heat recovered from the recuperator. This exergy is governed by a factor corresponds to

Fig. 15. The effect of the pressure ratio on the efficiency of the integrated system. Part A for SOFC-O option. Part B for SOFC-H option.
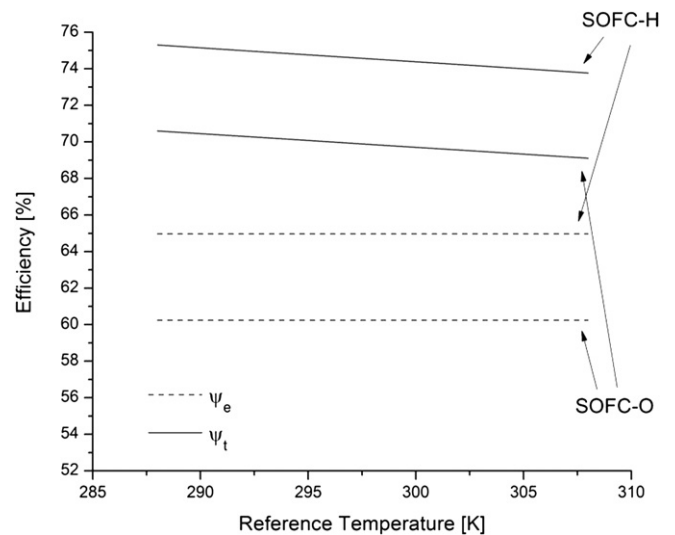

Fig. 16. Effect of reference temperature on the exergy efficiency of the system (base case).

efficiency of a Carnot engine operating between the temperature of the gaseous stream and the reference temperature. Hence, increasing the reference temperature reduces the amount of useful work potential of the heat recovery process resulting in lower total exergy efficiency.

6. Conclusions

This study has presented an innovative hybrid system, comprising of ammonia-fed solid oxide fuel cell integrated with a gas turbine power cycle. The simple yet effective configuration of the system allows makes it advantageous in combined heating, cooling and power applications.

The thermodynamic and the electrochemical processes of the system are modelled and validated, with excellent agreement, against experimental data obtained from the literature. In addition, a parametric investigation is performed to examine the effects of design and operating variables on the performance and thermodynamic efficiency of the system. It is evident from the results of the study that the overall system performance is affected by the configuration and arrangement of system components among other factors.

The highest exergy destruction found in the fuel cell can be attributed to the thermodynamic and electrochemical irreversibilities. The second highest exergy destruction occurs in heat exchanger (HX1), mainly due temperature mismatch between the incoming fluid streams.

In summary the hydrogen proton-conducting DA-SOFC demonstrates a better performance in comparison to the ion-conducting counterpart due to higher partial pressure of hydrogen at the anode under all operating conditions. Nonetheless, it is imperative to optimize all design and operating parameters to achieve the best possible performance and efficiency of the system.

Nomenclature

A	Area [m^2]
B_0	Permeability [m^2]
$\bar{c}_p$	Specific molar heat capacity [J mol^{-1} K^{-1}]
dx	Depth of electrode layer [m]
D^{eff}	Effective binary diffusion [m^2 s^{-1}]
D_k^{eff}	Effective Knudsen diffusion [m^2 s^{-1}]
$\bar{ex}$	Molar specific exergy [J mol^{-1}]
E	Reversible cell potential or voltage [V]
E^0	Standard cell potential or voltage [V]
$\dot{Ex}$	Exergy rate [W]
$\dot{Ex}_D$	Exergy destruction rate [W]
f	Fugacity of chemical species in the system
f^0	Fugacity of chemical species at STP
F	Faraday's constant (96,485 C mol^{-1})
$\bar{g}$	Specific molar Gibbs energy [J mol^{-1}]
G	Gibbs energy [J]
$\bar{g}^0$	Specific molar Gibbs energy at STP [J mol^{-1}]
$\bar{h}$	Specific molar enthalpy [J mol^{-1}]
H	Enthalpy [J]
H^0	Standard Enthalpy at STP [J]
H_c	Heat capacity rate [W K^{-1}]
I	Electric current [A]
J	Current density [A m^{-2}]
J_0	Exchange current density [A m^{-2}]
k	Ratio of specific molar heat
M	Molar mass [g mol^{-1}]
n	Number of moles [mol]
$\dot{n}$	Molar flow rate [mol s^{-1}]
N	Molar flux [mol m^{-2} s^{-1}]
p	Partial pressure [kPa]

P	Total pressure [kPa]
PR	Pressure ratio
Q	Heat [J]
$\dot{Q}$	Rate of heat transfer [W]
r_p	Mean pore radius of electrode [m]
$\bar{R}$	Gas constant [J mol^{-1} K^{-1}]
R_Ω	Electrolyte resistivity [Ω m]
$\bar{s}$	Molar specific entropy [J mol^{-1} K^{-1}]
S	Entropy [J K^{-1}]
T	Temperature [K]
U	Utilization [%]
ν	Specific molar volume [m^3 mol^{-1}]
V	Working potential or voltage [V]
W	Work [J]
$\dot{W}$	Work rate, power [W]
x	Molar ratio of produced hydrogen to consumed fuel
y	Molar fraction of chemical species
z	Number of electrons transferred per mole of fuel

Greek Letters

α	Charge transfer coefficient
Γ	Dimensionless temperature
δ	Electrolyte thickness [m]
Δ	Net change of quantity
ε	Porosity of electrode
ε/κ	Lennard-Jones temperature parameter [K]
η	Energy or thermal efficiency
μ	Viscosity [N s m^{-2}]
ξ	Heat exchanger effectiveness
σ	Molecular collision diameter [Å]
τ	Tortuosity of electrode
$\varphi_{\text{act, an}}$	Anode activation over-potential [V]
$\varphi_{\text{act, ca}}$	Cathode activation over-potential [V]
$\varphi_{\text{conc, an}}$	Anode concentration over-potential [V]
$\varphi_{\text{conc, ca}}$	Cathode concentration over-potential [V]
φ_Ω	Ohmic over-potential of electrolyte [V]
ψ	Exergy efficiency
Ω_D	Collision integral of diffusion

Subscripts

AC	Alternating current
amb	Ambient
c	Cold
ch	Chemical
C	Compressor
CC	Combustion chamber
CL	Cooling load
cmp	Component
DC	Direct current
e	Electric
eff	Effective
f	Fuel
FC	Fuel cell
G	Generator
h	Hot
HX	Heat exchanger
i	Chemical species
in	Inlet
INV	Inverter
j	Chemical species, system component
MC	Mixing chamber
min	Minimum
mix	Mixture
k	Knudsen diffusion
o	Oxidant

out   Outlet
T   Turbine
ph   physical
r   Reactants
REC   Recovery, Recuperator
s   Isentropic
T   Turbine

Acronyms

BWR   Back Work Ratio
CHP   Combined Heat and Power
CHCP   Combined Heating, Cooling and Power
DA-SOFC Direct Ammonia Solid Oxide Fuel Cell
DA-SOFC/GT Direct Ammonia Solid Oxide Fuel Cell Integrated with Gas Turbine
DGM   Dusty Gas Model
GEM   Gibbs Energy Minimization
LHV   Lower Heating Value
LSM-YSZ Lanthanum Strontium Manganite/Yttria-stabilized Zirconia
Ni-YSZ   Nickel/Yttria-stabilized Zirconia
SOFC/GT Solid Oxide Fuel Cell Integrated with Gas Turbine
SOFC-H   Hydrogen proton (H^+) conducting Solid Oxide Fuel Cell
SOFC-O   Oxygen ion (O^{2-}) conducting Solid Oxide Fuel Cell
STP   Standard Temperature and Pressure, 298 K and 101.325 kPa respectively
TPB   Triple-Phase Boundary
YSZ   Yttria-stabilized Zirconia

References

[1] Solid Oxide Fuel Cells: Technologies and Global Markets, BCC Research, Wellesley, MA, Report No.: EGY048B, 2011.
[2] F. Ishak, I. Dincer, C. Zamfirescu, Journal of Power Sources 202 (2012) 157–165.
[3] X. Zhang, S.H. Chan, G. Li, H.K. Ho, J. Li, Z. Feng, Journal of Power Sources 195 (2010) 685–702.
[4] C. Zamfirescu, I. Dincer, Thermochimica Acta 486 (2009) 32–40.
[5] I. Dincer, M.A. Rosen, C. Zamfirescu, Journal of Energy Resources Technology, Transactions of the ASME 131 (2009) 0320011–03200111.
[6] M.M. Mench, N.J. Hoboken, John Wiley & Sons, 2008, xi, p. 515.
[7] M. Ni, D.Y.C. Leung, M.K.H. Leung, Energy Conversion and Management 50 (2009) 268–278.
[8] A. Arpornwichanop, Y. Patcharavorachot, S. Assabumrungrat, Chemical Engineering Science 65 (2010) 581–589.
[9] S.H. Chan, C.F. Low, O.L. Ding, Journal of Power Sources 103 (2002) 188–200.
[10] R. Suwanwarangkul, E. Croiset, M.W. Fowler, P.L. Douglas, E. Entchev, M.A. Douglas, Journal of Power Sources 122 (2003) 9–18.
[11] V. Janardhanan, A Detailed Approach to Model Transport, Heterogeneous Chemistry, and Electrochemistry in Solid-oxide Fuel Cells, Universitätsverlag, Karlsruhe, 2007, (Online-Ressource).
[12] C.K. Ho, S.W. Webb, Gas Transport in Porous Media, Springer, Dordrecht, 2006.
[13] R.B. Bird, E.N. Lightfoot, W.E. Stewart, Transport Phenomena, second ed.. J. Wiley, New York; Toronto, 2002.
[14] B.E. Poling, J.M. Prausnitz, J.P. O'Connell, The Properties of Gases and Liquids, fifth ed.. McGraw-Hill, New York, 2001.
[15] H. Zhu, R.J. Kee, V.M. Janardhanan, O. Deutschmann, D.G. Goodwin, Journal of the Electrochemical Society 152 (2005) A2427–A2440.
[16] N.J. Themelis, Transport and Chemical Rate Phenomena, Gordon and Breach Publishers, Basel, Switzerland, 1995.
[17] H. Zhu, R.J. Kee, Journal of Power Sources 117 (2003) 61–74.
[18] M. Ni, D.Y.C. Leung, M.K.H. Leung, Journal of Power Sources 183 (2008) 682–686.
[19] Y. Patcharavorachot, W. Paengjuntuek, S. Assabumrungrat, A. Arpornwichanop, International Journal of Hydrogen Energy 35 (2010) 4301–4310.
[20] F. Krieth, M.S. Bohn, Principles of Heat Transfer, Brooks/Cole, Pacific Grove, USA, 2001.
[21] MATLAB, MathWorks Inc., Natick, MA, U.S.A, 2007.
[22] M.W. Chase, Journal of Physical and Chemical Reference Data (1998) Monograph, American Institute of Physics for the National Institute of Standards and Technology, New York.
[23] V. Hacker, K. Kordesch, Ammonia crackers, in: W. Vielstich, A. Lamm, H. Gasteiger (Eds.), Handbook of Fuel Cells — Fundamentals, Technology and Applications, John Wiley & Sons Ltd., Chichester, 2003, pp. 121–127.
[24] J. de Swaan Arons, H. van der Kooi, K. Sankaranarayanan, Efficiency and Sustainability in the Energy and Chemical Industries, CRC Press, 2004.
[25] Engineering Equation Solver V8.629, Madison, WI, U.S.A, 2010.
[26] R.Y. Chein, Y.C. Chen, C.S. Chang, J.N. Chung, International Journal of Hydrogen Energy 35 (2010) 589–597.
[27] EG & G. Services, U.S. Dept. of Energy, Office of Fossil Energy, National Energy Technology Laboratory, Morgantown, WV, 2004.
[28] Q. Ma, J. Ma, S. Zhou, R. Yan, J. Gao, G. Meng, Power Sources 164 (2007) 86–89.
[29] P.W. Li, M.K. Chyu, Journal of Heat Transfer 127 (2005) 1344–1362.
[30] A. Ringuedé, D. Bronine, J.R. Frade, Solid State Ionics 146 (2002) 219–224.
[31] M. Ni, D.Y.C. Leung, M.K.H. Leung, Journal of Power Sources 183 (2008) 687–692.
[32] K. Xie, Q. Ma, B. Lin, Y. Jiang, J. Gao, X. Liu, G. Meng, Journal of Power Sources 170 (2007) 38–41.
[33] A.V. Akkaya, International Journal of Energy Research 31 (2007) 79–98.